AIAA JOURNAL
Vol. 45, No. 7, July 2007

Computational Fluid Dynamics-Based Aeroservoelastic Analysis with Hyper-X Applications

K. K. Gupta*
NASA Dryden Flight Research Center, Edwards, California 93523
and
C. Bach†
Analytical Services and Materials, Inc., Edwards, California 93523

DOI: 10.2514/1.21992

A finite element computational fluids dynamics-based aeroservoelastic analysis methodology is presented in this paper, in which both structural and fluids discretization are achieved by the finite element method, and their interaction is modeled by the transpiration boundary condition technique. In the fluids discipline either inviscid or viscous flow may be accounted for, usually employing unstructured grids. A description of a novel viscous flow solver employing unstructured grids is given in detail. Provisions are made for digital as well as analog controllers. These new aeroservoelastic analysis techniques are next applied for the solution of a number of example problems including the novel Hyper-X launch vehicle. Experimental and actual flight test data are also compared with analysis results that signify to the efficacy and accuracy of the newly developed solution procedures.

Nomenclature

$\hat{\mathbf{C}}$	=	generalized damping matrix
$\mathbf{f}_a(t)$	=	generalized aerodynamic load vector
$\mathbf{f}_I(t)$	=	generalized impulse force vector
$\mathbf{f}_i$, $\mathbf{g}_i$	=	flux vector convection and diffusion terms
$\mathbf{G}_a$, $\mathbf{H}_a$, $\mathbf{C}_a$, $\mathbf{D}_a$	=	aerodynamic state-space matrices
$\mathbf{G}_c$, $\mathbf{H}_c$, $\mathbf{C}_c$, $\mathbf{D}_c$	=	controls state-space matrices
$\mathbf{G}_s$, $\mathbf{H}_s$, $\mathbf{C}_s$, $\mathbf{D}_s$	=	structural state-space matrices
$\hat{\mathbf{K}}$	=	generalized stiffness matrix
$\hat{\mathbf{M}}$	=	generalized mass matrix
$\mathbf{q}$	=	generalized displacement vector
t, T	=	time and temperature
$\mathbf{u}$	=	displacement vector
v	=	volume
$\boldsymbol{\delta}$	=	generalized displacement vector of the control surface
ρ	=	freestream density

Introduction

THE Hyper-X launch vehicle is a winged Pegasus booster rocket that carries the X-43 hypersonic flight research vehicle to an altitude of about 100,000 ft for a Mach 7 and a subsequent Mach 10 mission. A primary objective of the mission is to test the scramjet engine performance of the X-43 vehicle. The launch of the booster [1], carrying the X-43, is accomplished from a B-52 aircraft at a suitable altitude around 20,000 ft. These high performance flight vehicles are characterized by unprecedented levels of interactions among a number of major disciplines as structures, fluids, heat transfer, and controls engineering, among others, that may impose considerable constraint on dynamic stability and controls performance margins necessary for safety of flight. Thus an accurate computational fluid dynamics (CFD)-based simulation of these flight vehicles is of vital importance. Earlier effort in this direction relates to such an analysis pertaining to the X-43A [2] as well as the launch vehicle [3] at an elevation of 100,000 ft.

This paper first provides details of numerical techniques pertaining to the CFD, aeroelastic (AE), and (ASE) aeroservoelastic analyses. A common finite element (FE) discretization is effected for both the structural and the fluids continua and their interaction is simulated by adapting a transpiration boundary condition [4,5] strategy, in which the body normals are appropriately rotated to conform to the deformed structural shape. This method enables leaving the original aerodynamic mesh unchanged throughout the entire solution process, which may only need to be updated in the presence of large deformation. A number of verification problems are also solved to assess accuracy and efficiency of the associated code. This includes a simulation of flight of the Hyper-X vehicle along with a comparison of CFD solution and actual flight test data. Once launched from the B-52, the booster accelerates in a near horizontal flight, through the transonic flight regime, to eventually ascend to the desired 100,000 ft altitude for the X-43 flight. In this paper a novel CFD-based aeroelastic and aeroservoelastic analysis of the vehicle at transonic speed is presented in detail. The analysis is performed for the vehicle flight at Mach 0.9 and at an altitude of 22,500 ft and involves vibrations, CFD steady and unsteady flow simulation as well as stability solution. Such an analysis is further repeated at various altitudes to determine associated flutter boundary.

An aeroservoelastic analysis involves structural, CFD steady and unsteady flow, coupled fluids-structural, and fluids-structural-controls interaction simulations. Novel finite element based formulations pertaining to CFD, AE, and ASE analyses are presented herein in that order to present a systematic and cohesive solution methodology; finite element structural analysis employs widely available standard software and hence is not elaborated herein.

Numerical Solution of the Flow Equations

Many practical problems involve large scale computation and both spatial and temporal approximations are applied for the solution of the flow equations. A number of FE solution schemes [6,7] have been developed that are based on the Taylor–Galerkin (TG) formulation. Most of these schemes are characterized by somewhat higher CPU requirements primarily due to the use of predictor–corrector-type solution algorithms as well as evaluation of Jacobian-type matrices inherent in the formulation. The Taylor–Galerkin principles are also employed in the present formulation but without

Presented as Paper 884 at the AIAA Aerospace Science Conference and Exhibit, Reno, NV, 5–9 January 2004; received 22 December 2005; accepted for publication 12 August 2006.

*Staff, Research Engineering Directorate. Associate Fellow AIAA.
†Senior Engineer.

the higher order stabilization terms. A forward Euler time discretization is carried out in this procedure and the scheme is complimented by the addition of artificial dissipation, based on a pressure switch method, which aids in stabilizing the solution process and in capturing shocks. For viscous flow the inviscid solution is augmented with the viscous terms. The one equation model of turbulence [8] modeling has been found to be suitable for augmenting the finite element viscous flow solution [9].

The Navier–Stokes (N-S) equation in the absence of body forces takes the form,

$$\frac{\partial \mathbf{v}}{\partial t} + \frac{\partial \mathbf{F}_i}{\partial x_i} = 0, \qquad i = 1, 2, 3 \tag{1}$$

that may also be written as

$$\frac{\partial \mathbf{v}}{\partial t} + \frac{\partial \mathbf{f}_i}{\partial x_i} + \frac{\partial \mathbf{g}_i}{\partial x_i} = 0 \tag{2}$$

where the flux vector is split into convection $\mathbf{f}_i$ and diffusion $\mathbf{g}_i$ terms, and the diffusion can be expressed in terms of velocity gradients and viscosity. Other definitions pertaining to the conservation variables, flux, and body force column vectors, as well as the viscous stress are given as

$$\mathbf{v} = \begin{bmatrix} \rho & \rho u_j & \rho E \end{bmatrix}^T \qquad j = 1, 2, 3 \tag{3}$$

$$\mathbf{f}_i = \begin{bmatrix} \rho u_i & (\rho u_i u_j + p\delta_{ij}) & u_i(p + \rho E) \end{bmatrix}^T \qquad i = 1, 2, 3 \tag{4}$$

$$\mathbf{g}_i = \begin{bmatrix} 0 & \sigma_{ij} & \left(u_j \sigma_{ij} + k \frac{\partial T}{\partial x_i}\right) \end{bmatrix}^T \tag{5}$$

$$\mathbf{f}_b = \begin{bmatrix} 0 & f_{bj} & u_j f_{bj} \end{bmatrix}^T \tag{6}$$

$$\sigma_{ij} = \mu \left[\frac{\partial u_i}{\partial x_j} + \frac{\partial u_j}{\partial x_i} - \frac{2}{3} \frac{\partial u_l}{\partial x_l} \delta_{ij} \right] \qquad l = 1, 2, 3 \tag{7}$$

where u_j are velocity components in the x_j coordinate system; ρ, p, and E are the density, pressure, and total energy, respectively; μ is the dynamic viscosity; k is the thermal conductivity, the heat flux q_j being $-k\partial T/\partial x_j$; T is the temperature; f_b represents the body forces, and δ_{ij} is the Kronecker delta ($=1, i = j, =0, i \neq j$). The energy equation in compressible flow is coupled with other governing flow equations. The coupling is accomplished through the perfect gas law

$$p = \rho R T \tag{8}$$

where R is the gas constant. For the isentropic assumption the speed of sound and the density and pressure are related as

$$c^2 = \frac{\gamma p}{\rho} = \gamma R T \tag{9}$$

and density and pressure are related by the equation

$$\frac{\partial \rho}{\partial t} = \frac{\partial \rho}{\partial p} \frac{\partial p}{\partial t} = \frac{1}{c^2} \frac{\partial p}{\partial t} \tag{10}$$

in which $\gamma = c_p/c_v$ and c_p is the specific heat at constant pressure, with c_v being the specific heat at constant volume.

Taylor's expansion of the solution $v(x, t)$ in the time domain takes the form

$$\mathbf{v}(t + \Delta t) = \mathbf{v}(t) + \frac{\partial \mathbf{v}(t)}{\partial t} \Delta t + \frac{1}{2} \frac{\partial^2 \mathbf{v}(t)}{\partial t^2} \Delta t^2 + \cdots \tag{11}$$

and neglecting the second order term, Eq. (11) is written as

$$\Delta \mathbf{v} = -\Delta t \left[\frac{\partial \mathbf{F}_i}{\partial x_i} \right]_{(t)} = -\Delta t \left[\frac{\partial \mathbf{f}_i}{\partial x_i} + \frac{\partial \mathbf{g}_i}{\partial x_i} \right]_{(t)} \tag{12}$$

where $\Delta \mathbf{v} = \mathbf{v}(t + \Delta t) - \mathbf{v}(t)$. Next applying Galerkin's spatial idealization $\mathbf{v} = \mathbf{N}\tilde{\mathbf{v}}$, with $\tilde{\mathbf{v}}$ being the nodal values, and $\mathbf{N}$ the shape function and assuming absence of body forces, Eq. (12) takes the following form:

$$\mathbf{M}\Delta\tilde{\mathbf{v}} = -\Delta t \left[\frac{\partial u_i}{\partial x_i} \mathbf{M} + \mathbf{K} \right] \tilde{\mathbf{v}} - \Delta t(\hat{\mathbf{f}}_1 + \hat{\mathbf{f}}_2) + \Delta t \hat{\mathbf{R}} + \Delta t(\mathbf{K}_\sigma + \mathbf{f}_\sigma) \tag{13}$$

where $\mathbf{M}$ is the consistent mass matrix, $\mathbf{K}$ the convection matrix, $\hat{\mathbf{f}}_1$, $\hat{\mathbf{f}}_2$ the pressure matrices, $\mathbf{K}_\sigma$ the second order matrix that includes viscous and heat flux effects, and $\mathbf{f}_\sigma$ the boundary integral matrix from second order terms; the individual matrices are defined as

$$\mathbf{M} = \int_v \mathbf{N}^T \mathbf{N} \, dV; \qquad \mathbf{K} = \int_v \mathbf{N}^T \bar{u}_i \frac{\partial \mathbf{N}}{\partial x_i} \, dV$$

$$\hat{\mathbf{f}}_1 = \int_v \mathbf{N}^T \bar{p}_i \frac{\partial \mathbf{e}_i}{\partial x_i} \, dV; \qquad \hat{\mathbf{f}}_2 = \int_v \mathbf{N}^T \bar{\mathbf{e}}_i \frac{\partial p_i}{\partial x_i} \, dV$$

$$\mathbf{K}_\sigma = -\int_v \frac{\partial \mathbf{N}^T}{\partial x_j} \mathbf{e}_j \sigma_{ij} \, dV - \int_v \frac{\partial \mathbf{N}^T}{\partial x_i} \mathbf{m}_j \hat{q}_j \, dV$$

$$\mathbf{f}_\sigma = \int_\Gamma \mathbf{N}^T \mathbf{e}_j \sigma_{ij} \hat{\mathbf{n}} \, d\Gamma + \int_\Gamma \mathbf{N}^T \mathbf{m}_j \hat{q}_j \hat{\mathbf{n}}_j \Gamma \tag{14}$$

In the above equations, $\bar{p}_i$, $\bar{u}_i$, $\bar{\mathbf{e}}_i$ are the average values; $\mathbf{e}_1 = \begin{pmatrix} 0 & 1 & 0 & 0 & u_1 \end{pmatrix}^T$, $\mathbf{e}_2 = \begin{pmatrix} 0 & 0 & 1 & 0 & u_2 \end{pmatrix}^T$, $\mathbf{e}_3 = \begin{pmatrix} 0 & 0 & 0 & 1 & u_3 \end{pmatrix}^T$, $\hat{\mathbf{R}}$ [Eq. (23)] is the artificial dissipation and $\mathbf{m}_1 = \mathbf{m}_2 = \mathbf{m}_3 = \begin{bmatrix} 0 & 0 & 0 & 0 & 1 \end{bmatrix}^T$; $\hat{q}_j$ is the heat flux in the energy equation. The viscous effects may be modified to include turbulence terms.

The solution for the flow equation is achieved by a two step algorithm, the inviscid solution being augmented with the viscous term and stabilized with the artificial dissipation term. Expressing

$$\Delta\tilde{\mathbf{v}} = \tilde{\mathbf{v}}_{n+1} - \tilde{\mathbf{v}}_n \tag{15}$$

then, Eq. (13) takes the form

$$\mathbf{M}(\tilde{\mathbf{v}}_{n+1} - \tilde{\mathbf{v}}_n) = \frac{-\Delta t}{2} [c\mathbf{M} + \mathbf{K}](\tilde{\mathbf{v}}_{n+1} + \tilde{\mathbf{v}}_n) - \Delta t(\hat{\mathbf{f}}_1 + \hat{\mathbf{f}}_2) \tag{16}$$

which becomes

$$\left[\left(1 + \frac{\Delta t}{2} c\right) \mathbf{M} + \frac{\Delta t}{2} \mathbf{K} \right] \tilde{\mathbf{v}}_{n+1} = \left[\left(1 - \frac{\Delta t}{2} c\right) \mathbf{M} - \frac{\Delta t}{2} \mathbf{K} \right] \tilde{\mathbf{v}}_n + \Delta t \mathbf{R} \tag{17}$$

or

$$[\mathbf{M}_+]\tilde{\mathbf{v}}_{n+1} = [\mathbf{M}_-]\tilde{\mathbf{v}}_n + \Delta t \mathbf{R} \tag{18}$$

where

$$\mathbf{R} = -(\hat{\mathbf{f}}_1 + \hat{\mathbf{f}}_2), \qquad c = \partial u_i / \partial x_i \tag{19}$$

Writing

$$\mathbf{M}_+ = \mathbf{D}_+ + \mathbf{M}'_+ \tag{20}$$

with the matrix $\mathbf{D}_+$ having diagonal elements, then Eq. (18) may be solved as follows:

Step 1: Assemble

$$[\mathbf{D}_+]\tilde{\mathbf{v}}_{n+1} = [\mathbf{M}_-]\tilde{\mathbf{v}}_n - [\mathbf{M}'_+]\tilde{\mathbf{v}}_{n+1} + \Delta t \mathbf{R} \tag{21}$$

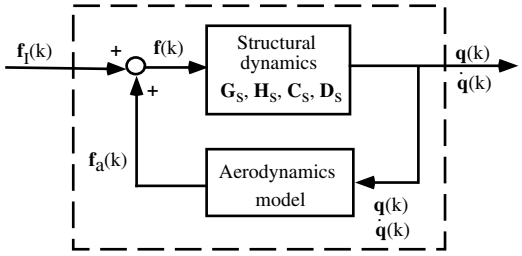

Fig. 1 Coupled AE model.

Step 2: Solve $\tilde{\mathbf{v}}_{n+1}$ iteratively

$$\tilde{\mathbf{v}}_{n+1}^{(i+1)} = [\mathbf{D}_+]^{-1}\left\{[\mathbf{M}_-]\tilde{\mathbf{v}}_\mathbf{n} - [\mathbf{M}'_+]\tilde{\mathbf{v}}_{n+1}^{(i)} + \Delta t(\mathbf{R} + \hat{\mathbf{R}} + \mathbf{K}_\sigma + \mathbf{f}_\sigma)\right\} \tag{22}$$

Step 3: If $\|\tilde{\mathbf{v}}_{n+1}^{(i+1)}\| \neq \text{EPS1}\|\tilde{\mathbf{v}}_{n+1}^{(i)}\|$ go to step 2.
Step 4: If $\|\tilde{\mathbf{v}}_{n+1}\| \neq \text{EPS2}\|\tilde{\mathbf{v}}_n\|$ go to step 1.
Step 5: Repeat steps 1 to 4 NITER (required number of solution iteration steps) times until convergence is reached, that is until $\tilde{\mathbf{v}}_{n+1} \approx \tilde{\mathbf{v}}_n$; EPS1 and EPS2 are suitable convergence factors.

The iterative solution in step 2 takes a small number of steps, usually 1 or 2 to achieve convergence.

An artificial dissipation term is applied in regions of high gradients to prevent oscillations in the vicinity of discontinuities by incorporating pressure switched diffusion coefficients appropriately. Then,

$$\hat{\mathbf{R}} = \frac{C_S S_e}{\Delta t}\mathbf{M}_L^{-1}[\mathbf{M}_c - \mathbf{M}_L]\tilde{\mathbf{v}}_n \tag{23}$$

where C_S is a shock capturing constant, S_e is the averaged element value of the nodal pressure switch given as

$$S_i = \frac{|\Sigma(p_i - p_j)|}{\Sigma(|p_i - p_j|)} \tag{24}$$

and $\mathbf{M}_c$ and $\mathbf{M}_L$ are consistent and lumped mass matrices, respectively; i is the node under consideration, and j are the nodes connected to i.

To compute the viscous components, σ_{ij} in Eq. (14) is written as

$$\sigma_{ij} = -\frac{2}{3}\frac{\mu}{Re}\frac{\partial u_l}{\partial x_l}\delta_{ij} + \frac{\mu}{Re}\left(\frac{\partial u_i}{\partial x_j} + \frac{\partial u_j}{\partial x_i}\right) \tag{25}$$

and the diffusion flux of the Navier–Stokes equation is

$$g_i = \begin{pmatrix} 0 & \sigma_{i1} & \sigma_{i2} & \sigma_{i3} & u_j\sigma_{ij} + \frac{1}{RePr}\frac{\partial T}{\partial x_i} \end{pmatrix}^T \qquad i = 1,2,3; \quad j = 1,2,3 \tag{26}$$

in which μ is the nondimensional viscosity term, and Re and Pr are the Reynolds and Prandtl numbers, respectively. The components of $\partial g_i/\partial x_i$ are evaluated term by term which are then discretized by Galerkin approximation. It is apparent from Eq. (26) that the second order terms occur only in momentum and energy equations. The

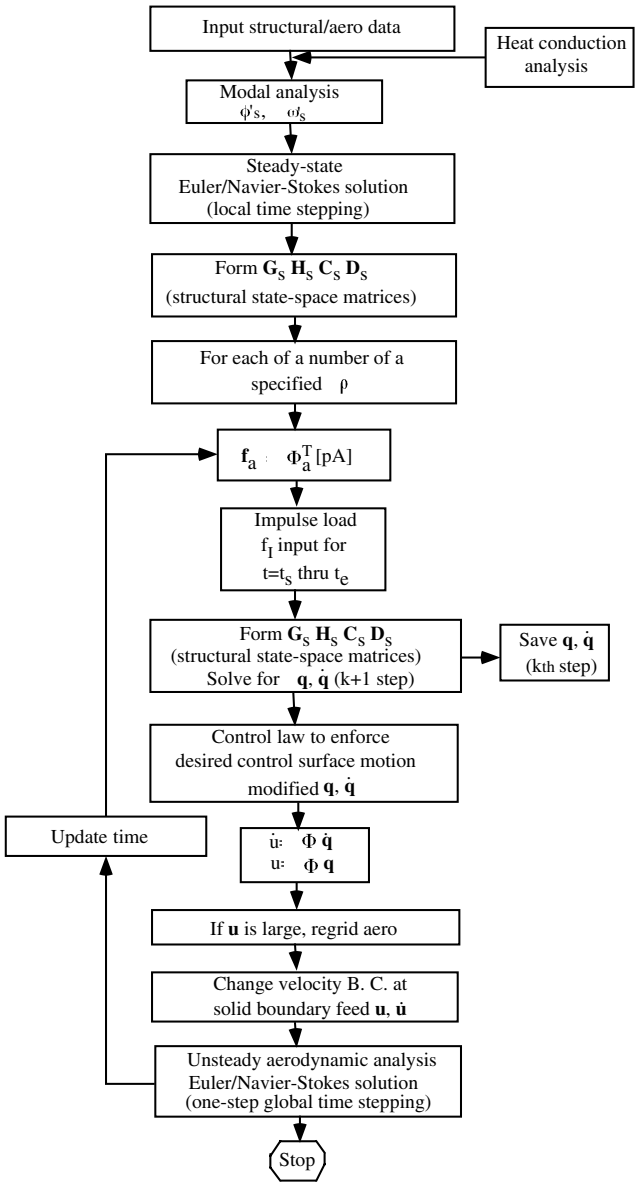

Fig. 2 Nonlinear AE/ASE analysis methodology.

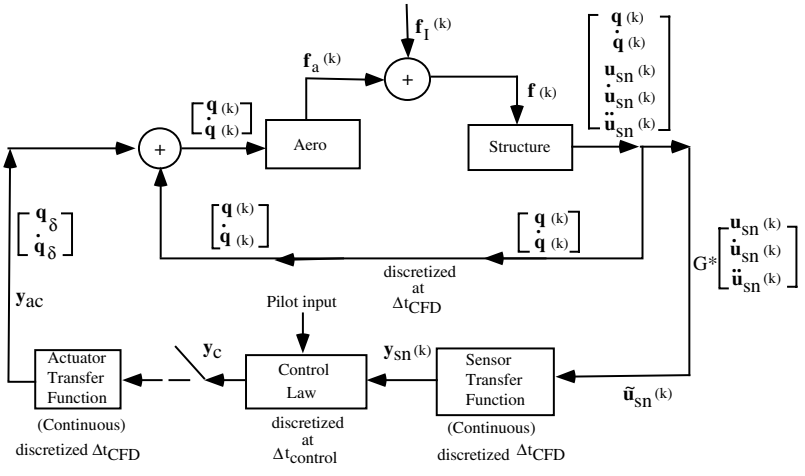

Fig. 3 Coupled aeroservoelastic model.

three momentum equations will have seven terms each, whereas the energy equation will have 24 terms. Thus, for example, the x_1 momentum component equation can be written as

$$\frac{\partial \sigma_{i1}}{\partial x_i} = \frac{\partial \sigma_{11}}{\partial x_1} + \frac{\partial \sigma_{21}}{\partial x_2} + \frac{\partial \sigma_{31}}{\partial x_3} = \frac{\mu}{Re}\frac{\partial}{\partial x_1}\left[\frac{4}{3}\frac{\partial u_1}{\partial x_1} - \frac{2}{3}\frac{\partial u_2}{\partial x_2} - \frac{2}{3}\frac{\partial u_3}{\partial x_3}\right] + \frac{\mu}{Re}\frac{\partial}{\partial x_2}\left[\frac{\partial u_2}{\partial x_1} + \frac{\partial u_1}{\partial x_2}\right] + \frac{\mu}{Re}\frac{\partial}{\partial x_3}\left[\frac{\partial u_1}{\partial x_3} + \frac{\partial u_3}{\partial x_1}\right] \tag{27}$$

Each of these equations when discretized by the Galerkin method yields the viscous contribution. For each of the four nodes, three components of the viscous terms can be written as

$$\begin{bmatrix} \mathrm{VIN(I1)} \\ \mathrm{VIN(I1+1)} \\ \mathrm{VIN(I1+2)} \end{bmatrix} = \frac{\Delta t \mu}{Re} V \begin{bmatrix} (J_{1i} \quad J_{2i} \quad J_{3i})(\sigma_{11} \quad \sigma_{12} \quad \sigma_{13})^T \\ (J_{2i} \quad J_{1i} \quad J_{3i})(\sigma_{22} \quad \sigma_{12} \quad \sigma_{23})^T \\ (J_{3i} \quad J_{2i} \quad J_{1i})(\sigma_{33} \quad \sigma_{32} \quad \sigma_{31})^T \end{bmatrix} \qquad i = 1, \ldots, 4 \tag{28}$$

in which I1 = 2, 7, 12, and 17, respectively, for the momentum equation. The remaining terms of the energy equation are as follows:

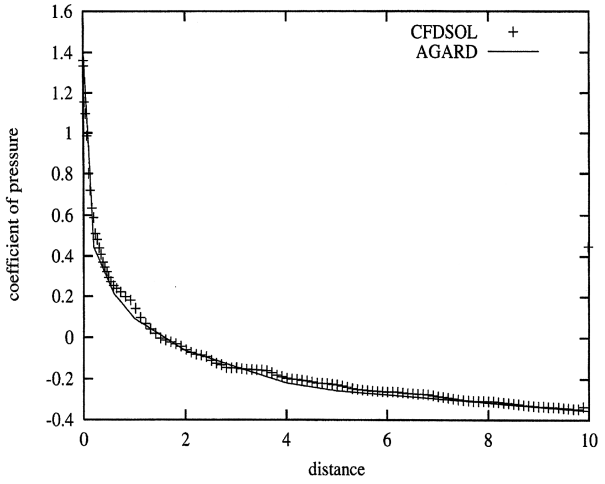

Fig. 4 C_p distribution along the surface of the NACA0012 aerofoil, inviscid flow.

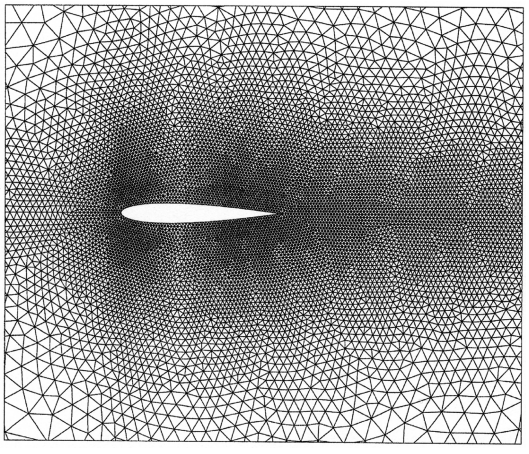

Fig. 5 Finite element mesh for supersonic viscous flow past a NACA0012 aerofoil.

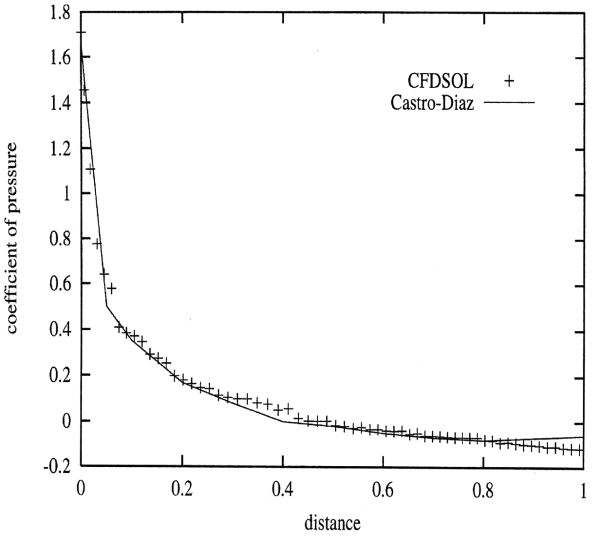

Fig. 6 Distribution of C_p for viscous supersonic flow, $Re = 10,000$, $M = 2$.

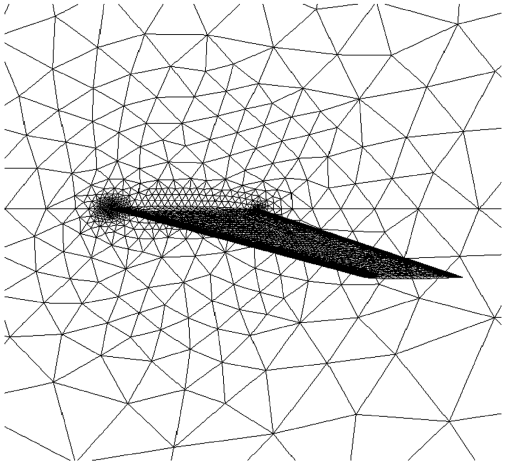

Fig. 7 Partial view of the CFD surface grid for the AGARD wing and the symmetry plane.

$$\mathrm{VIN}\,(5) = \sum_{i=1}^{3} J_{i1}\left[X_i C_1 + \left(\sum_{j=1}^{4} T_{ij}\right) c_2\right] \tag{29}$$

$$\mathrm{VIN}\,(10) = \sum_{i=1}^{3} J_{i2}\left[X_i C_1 + \left(\sum_{j=1}^{4} T_{ij} c_2\right)\right] \tag{30}$$

$$\mathrm{VIN}\,(15) = \sum_{i=1}^{3} J_{i3}\left[X_i C_1 + \left(\sum_{j=1}^{4} T_{ij}\right) c_2\right] \tag{31}$$

Table 1 Comparison of calculated and test results for the AGARD wing

Freestream M	Flutter speed index			Flutter frequency ratio	
	STARS	Ref. [18]	Test	STARS	Test
0.499	0.453	0.438	0.446	0.567	0.535
0.678	0.429	0.418	0.417	0.494	0.472
0.900	0.362	0.3625	0.370	0.409	0.422
0.960	0.334	0.3010	0.308	0.363	0.365
1.072	0.302	0.425	0.320	0.388	0.362
1.141	0.410	0.6375	0.403	0.447	0.459

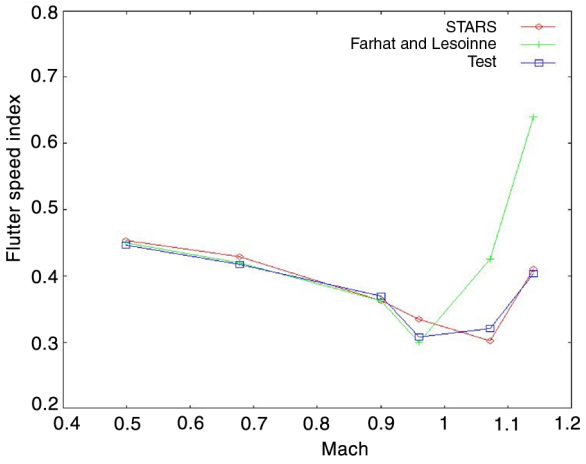

a) Flutter speed index vs Mach number

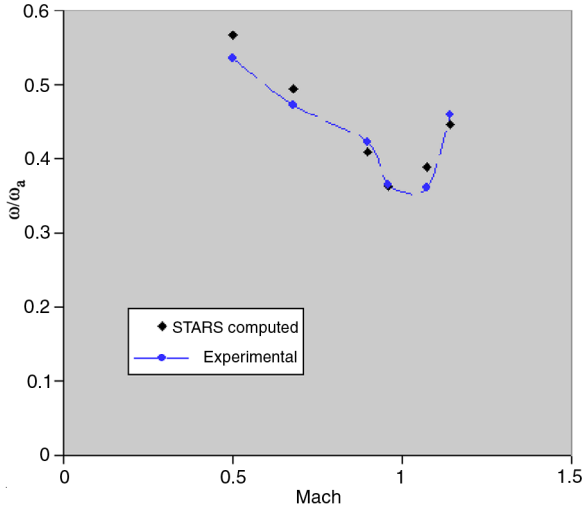

b) Flutter frequency ratio vs Mach number

Fig. 8 Comparison of analysis and test data for AGARD 445.6.

$$\text{VIN}\,(20) = \sum_{i=1}^{3} J_{i4}\left[X_i C_1 + \left(\sum_{j=1}^{4} T_{ij}\right) c_2\right] \tag{32}$$

in which

$$X_1 = \bar{u}\sigma_{11} + \bar{v}\sigma_{12} + \bar{\omega}\sigma_{13} \qquad X_2 = \bar{u}\sigma_{21} + \bar{v}\sigma_{22} + \bar{\omega}\sigma_{23}$$
$$X_3 = \bar{u}\sigma_{31} + \bar{v}\sigma_{32} + \bar{\omega}\sigma_{33} \tag{33}$$

and

$$c_1 = \frac{\Delta t \mu}{Re} V, \qquad c_2 = \frac{\Delta t}{RePr} V, \qquad T_{ij} = \left[\frac{\partial \mathbf{N}_j}{\partial x_i}\right]^T \left[\frac{\partial \mathbf{N}_j}{\partial x_i}\right] \tag{34}$$

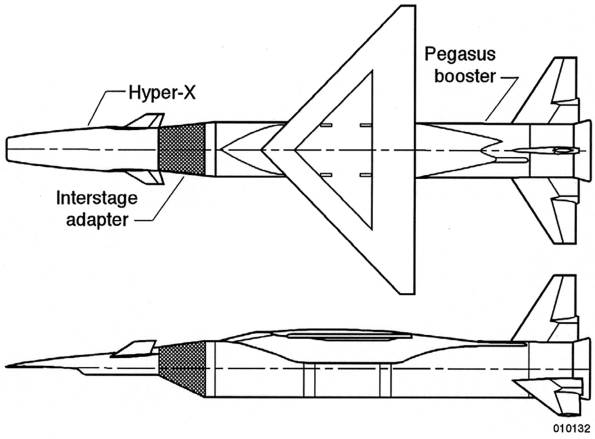

Fig. 9 Hyper-X flight vehicle.

with **J** being the Jacobian matrix. For turbulent flow, μ is replaced by $\mu + \mu_t$, k by $k + (\mu_t c_p)/(Pr_t)$, and c_1 and c_2 take the forms,

$$c_1 = \frac{\Delta t}{R_e} V(\mu + \mu_t); \qquad c_2 = \frac{\Delta t}{Re} V\left[\frac{1}{Pr_t} + \frac{\mu_t}{Pr_t}\right] \tag{35}$$

in which $\bar{u}$, $\bar{v}$, and $\bar{\omega}$ are the average velocity values in an element; μ_t is the turbulent viscosity, and Pr_t is the turbulent Prandtl number. For turbulence [8] modeling, a one equation model has been implemented in the STARS program.

Time Marched Aeroelastic and Aeroservoelastic Analyses

For the nonlinear aeroelastic and aeroservoelastic analyses [10,11], both the fluid and solids domains are idealized by the common finite element method. Figure 1 depicts a coupled aeroelastic model, whereas Fig. 2 shows the flow chart of the numerical algorithm adopted in the STARS [10] program for the CFD-based, integrated, aerostructural-controls analysis of structures such as aerospace vehicles; a corresponding coupled aeroservoelastic model is shown in Fig. 3. This procedure starts with the finite element structural modeling and subsequently computes the natural frequencies ω and modes ϕ, incorporating rigid-body, elastic, and control-surface motions, by solving

$$\mathbf{M}\ddot{\mathbf{u}} + \mathbf{K}\mathbf{u} = 0 \tag{36}$$

in which **M** and **K** are the inertial and stiffness matrices, respectively, and **u** is the displacement vector. Next, a steady-state Euler/N-S solution is effected using the local time-stepping, two step solution procedure described earlier. An associated vehicle equation of motion is then cast into the frequency domain as

$$\hat{\mathbf{M}}\ddot{\mathbf{q}} + \hat{\mathbf{C}}\dot{\mathbf{q}} + \hat{\mathbf{K}}\mathbf{q} + \mathbf{f}_a(t) + \mathbf{f}_I(t) = 0 \tag{37}$$

in which the generalized matrices and vectors are as follows: **q** is the displacement vector ($=\mathbf{\Phi}^T\mathbf{u}$), $\hat{\mathbf{M}}$ the inertia matrix ($=\mathbf{\Phi}^T\mathbf{M}\mathbf{\Phi}$), and,

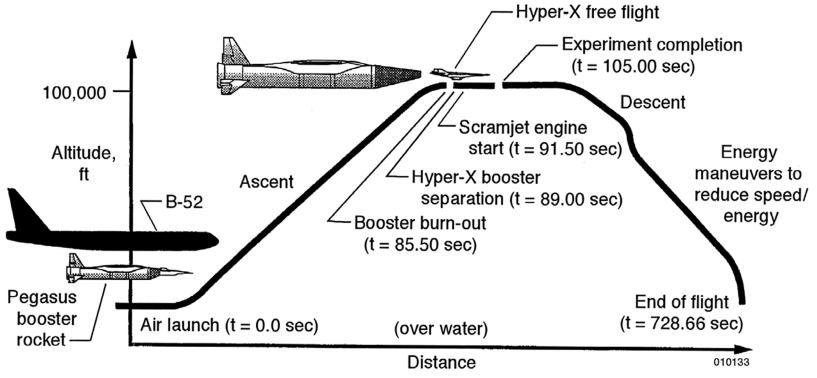

Fig. 10 Hyper-X flight trajectory.

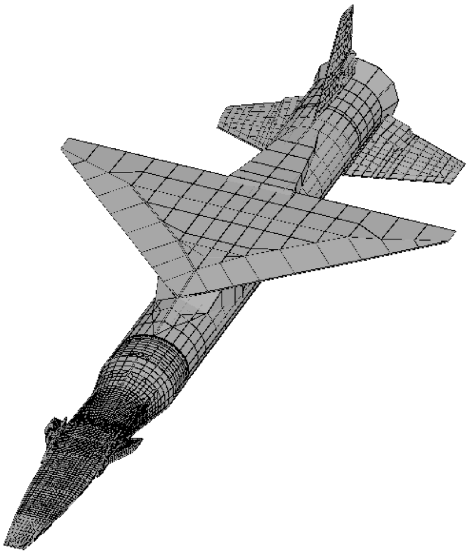

Fig. 11 Hyper-X finite element structural model.

similarly, $\hat{\mathbf{K}}$, $\hat{\mathbf{C}}$ the stiffness and damping matrices; $\mathbf{f}_a(t)$ the aerodynamic (CFD) load vector ($=\mathbf{\Phi}_a^T pA$), p is the fluid pressure at a fluid node, and A is the appropriate surface area around the node; $\mathbf{\Phi}_a$ is the modal vector at aerodynamic grid points on the vehicle surface, interpolated from relevant structural modes; and $\mathbf{f}_I(t)$ is the applied generalized structural impulse force vector.

A state-space matrix equation form of Eq. (37) is written as

$$\begin{bmatrix} \mathbf{I} & 0 \\ 0 & \mathbf{I} \end{bmatrix} \begin{bmatrix} \dot{\mathbf{q}} \\ \ddot{\mathbf{q}} \end{bmatrix} - \begin{bmatrix} 0 & \mathbf{I} \\ -\hat{\mathbf{M}}^{-1}\hat{\mathbf{K}} & -\hat{\mathbf{M}}^{-1}\hat{\mathbf{C}} \end{bmatrix} \begin{bmatrix} \mathbf{q} \\ \dot{\mathbf{q}} \end{bmatrix} - \begin{bmatrix} 0 \\ -\hat{\mathbf{M}}^{-1}\mathbf{f}_a(t) \end{bmatrix} - \begin{bmatrix} 0 \\ -\hat{\mathbf{M}}^{-1}\mathbf{f}_I(t) \end{bmatrix} = 0 \tag{38}$$

or

$$\dot{\mathbf{x}}_s(t) = \mathbf{A}_{st}\mathbf{x}_s(t) + \mathbf{B}_{st}\mathbf{f}(t) \tag{39}$$

where

$$\mathbf{B}_{st} = \begin{bmatrix} 0 \\ -\hat{\mathbf{M}}^{-1} \end{bmatrix}, \qquad \mathbf{f}(t) = \mathbf{f}_a(t) + \mathbf{f}_I(t), \qquad \mathbf{x}_s(t) = \begin{bmatrix} \mathbf{q} \\ \dot{\mathbf{q}} \end{bmatrix} \tag{40}$$

and

$$\mathbf{y}_s(t) = \mathbf{C}_{st}\mathbf{x}_s(t) + \mathbf{D}_{st}\mathbf{f}(t) \tag{41}$$

in which $\mathbf{C}_{st} = \mathbf{I}$ and $\mathbf{D}_{st} = 0$.

Following the procedure of linear aeroservoelasticity [10], Eq. (41) may be modified to account for the presence of sensors

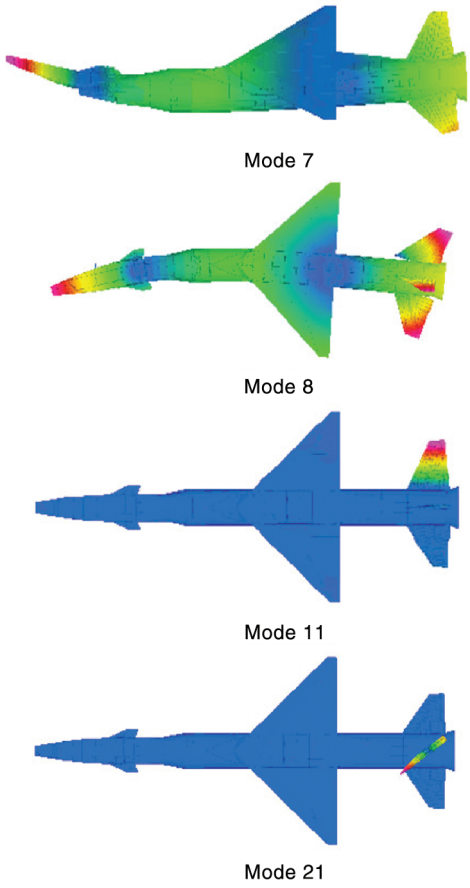

Fig. 12 Hyper-X typical elastic mode shapes.

$$\begin{Bmatrix} \mathbf{q}(t) \\ \dot{\mathbf{q}}(t) \\ \mathbf{u}_{sn}(t) \\ \dot{\mathbf{u}}_{sn}(t) \\ \ddot{\mathbf{u}}_{sn}(t) \end{Bmatrix} = \begin{bmatrix} \mathbf{I} & 0 \\ 0 & \mathbf{I} \\ \mathbf{T}_{sn}\mathbf{\Phi} & 0 \\ 0 & \mathbf{T}_{sn}\mathbf{\Phi} \\ -\mathbf{T}_{sn}\mathbf{\Phi}\hat{\mathbf{M}}^{-1}\hat{\mathbf{K}} & -\mathbf{T}_{sn}\mathbf{\Phi}\hat{\mathbf{M}}^{-1}\hat{\mathbf{C}} \end{bmatrix} \begin{Bmatrix} \mathbf{q}(t) \\ \dot{\mathbf{q}}(t) \end{Bmatrix} + \begin{Bmatrix} 0 \\ 0 \\ 0 \\ 0 \\ -\mathbf{T}_{sn}\mathbf{\Phi}\hat{\mathbf{M}}^{-1} \end{Bmatrix} \mathbf{f}(t) \tag{42}$$

or

$$\mathbf{y}_{ss}(t) = \mathbf{C}_{ss}\mathbf{x}_s(t) + \mathbf{D}_{ss}\mathbf{f}(t) \tag{43}$$

Table 2 Hyper-X stack free vibration analysis results

Mode	STARS freq., Hz $\alpha_v = 12.43$ deg, $\alpha_{HT} = -11$ deg	Mode shape description (major motion)	Modes for AE analysis	Modes for ASE analysis
1–6	0.0	Rigid-body modes		1–6
7 (1st el)	8.03	F1B vertical (S)	7	7
8 (2 el)	9.44	F1B lateral (A/S)	8	8
9 (3 el)	11.42	RT FIN F/A	——	
10 (4 el)	11.99	LT FIN F/A	——	
11 (5 el)	13.21	RT FIN 1B	11	11
12 (6 el)	14.20	RUDDER 1B	12	12
13 (7 el)	14.45	LT FIN 1/B	13	13
14 (8 el)	15.05	RUDDER F/A	——	
15 (9 el)	16.38	F2B vertical (S)	15	15
21 (15 el)	28.97	RUDDER 1/T	21	21
CL	0.0	Control longitudinal rigid-body mode		CL

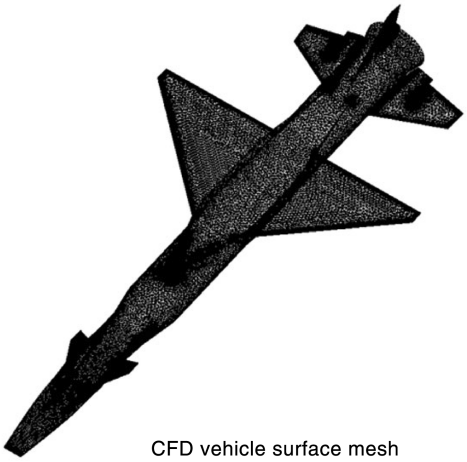

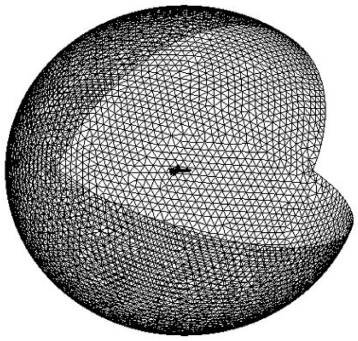

Fig. 13 Hyper-X CFD surface and global mesh.

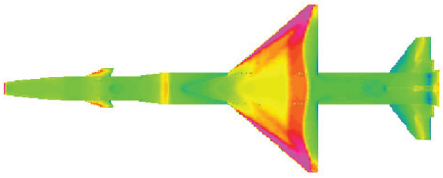

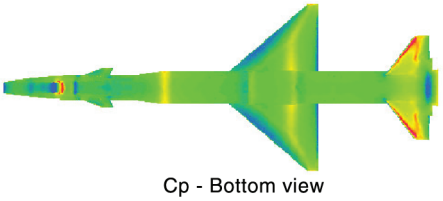

Fig. 14 Hyper-X Mach and pressure distribution.

where the vectors $\mathbf{u}_{sn}$ denote the real, physical displacements of the sensors in the continuous time domain. Also the interpolation matrix $\mathbf{T}_{sn}$, having sensor location information, is of dimensions ($2 \times$ NS, N), with NS being the number of sensors, and N being the number of degree of freedom for the structure. Equation (43) is the sensor output

Table 3 Comparison of computed and flight test measured pressure data for the Hyper-X

Sensor point	Pressure, psi		
	Flight test	CFD computed	Percent difference
001	1.6900	1.7297	2.34
003	1.7800	1.6890	6.12
007	−0.2419	−0.1400	42.12
085	−0.1567	−0.3886	147.99
090	0.07	−0.08	2.56

relationship signifying motion at the sensors due to the body motion $\mathbf{C}_{ss}$ and control motion $\mathbf{D}_{ss}$. These equations are next converted from inertial to body axis frame

$$\dot{\mathbf{x}}_s(t) = \tilde{\mathbf{T}}_2^{-1}(\mathbf{A}_{st}\tilde{\mathbf{T}}_1 - \tilde{\mathbf{T}}_3)\mathbf{x}_s(t) + \tilde{\mathbf{T}}_2^{-1}\mathbf{B}_{st}\mathbf{f}(t) \tag{44}$$

$$\mathbf{y}_s(t) = \mathbf{C}_{ss}\tilde{\mathbf{T}}_1\mathbf{x}_s(t) + \mathbf{D}_{ss}\mathbf{f}(t) \tag{45}$$

which may then be written as

$$\dot{\mathbf{x}}_s(t) = \mathbf{A}_s\mathbf{x}_s(t) + \mathbf{B}_s\mathbf{f}(t) \tag{46}$$

$$\mathbf{y}_s(t) = \mathbf{C}_s\mathbf{x}_s(t) + \mathbf{D}_s\mathbf{f}(t) \tag{47}$$

in which $\tilde{\mathbf{T}}_1$ and $\tilde{\mathbf{T}}_2$ are coordinate transformation matrices of dimensions (NR2 $\times$ NR2); NR2 $= 2 \times$ NR, with NR being the number of desired roots. These equations are then converted to the zero-order hold (ZOH) discrete time equivalent at the kth step:

$$\mathbf{x}_s(k+1) = \mathbf{G}_s\mathbf{x}_s(k) + \mathbf{H}_s\mathbf{f}(k) \tag{48}$$

$$\mathbf{y}_s(k) = \mathbf{C}_s\mathbf{x}_s(k) + \mathbf{D}_s\mathbf{f}(k) \tag{49}$$

where

$$\mathbf{G}_s = e^{\mathbf{A}_s\Delta t} \quad \text{and} \quad \mathbf{H}_s(k) = [e^{\mathbf{A}_s\Delta t} - \mathbf{I}][\mathbf{A}_s^{-1}\mathbf{B}_s] \tag{50}$$

$$\mathbf{f}(k) = \mathbf{f}_a(k) + \mathbf{f}_I(k) \tag{51}$$

and $\Delta t = t_{k+1} - t_k$,, and $\mathbf{C}_s$ and $\mathbf{D}_s$ remain unchanged.

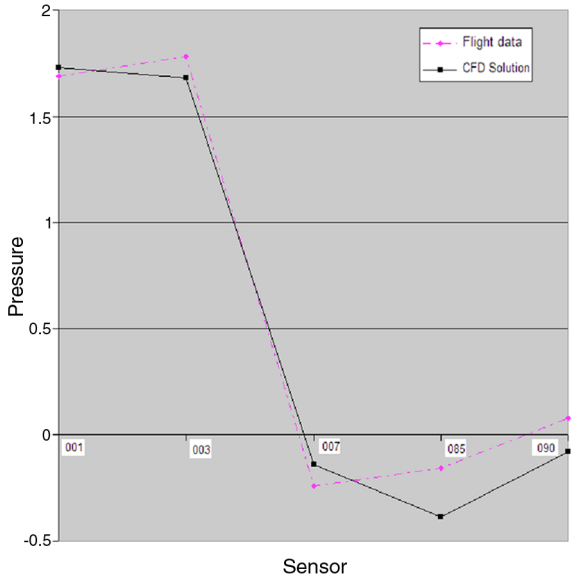

Fig. 15 Comparison of flight measured and calculated (CFD) pressure data.

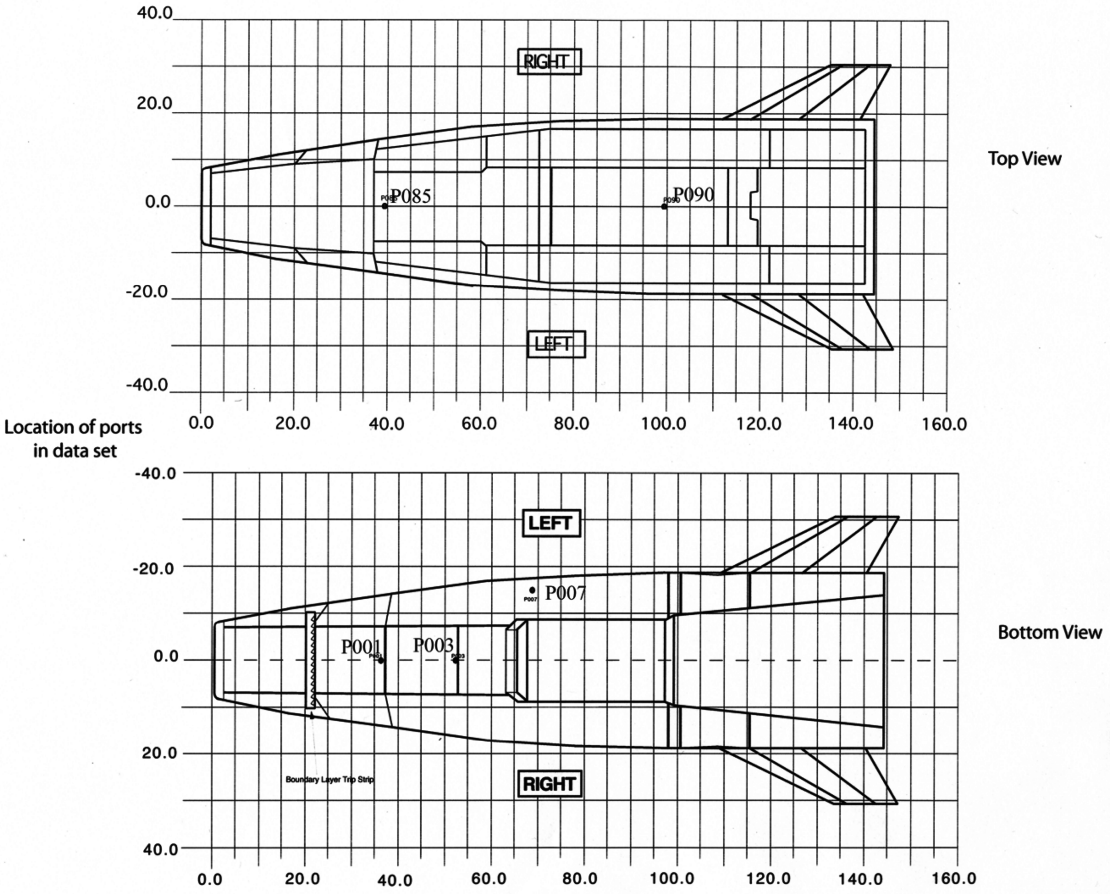

Fig. 16 Hyper-X sensor locations on X-43.

The related ASE analysis procedure is depicted in Fig. 3, where the generalized displacement $\mathbf{q}$ is defined as

$$\mathbf{q} = \begin{pmatrix} \mathbf{q}_R & \mathbf{q}_E & \mathbf{q}_\delta \end{pmatrix}^T \tag{52}$$

in which $\mathbf{q}_R$, $\mathbf{q}_E$, and $\mathbf{q}_\delta$ are the generalized rigid-body, elastic, and control-surface displacements, respectively. Thus the continuous aerostructural outputs are converted to a discrete time equivalent form using the time interval Δt_{CFD}. Other continuous systems such as the sensor and the actuator transfer functions are also discretized using the time interval Δt_{CFD}. The digital control law has its own sampling rate Δt_C and it only participates in the solution when the two sampling rates coincide. The sensor motions can be obtained from Eq. (49), through the gain matrix $\mathbf{G}$, as

$$\tilde{\mathbf{u}}_{sn} = \mathbf{G}\mathbf{y}_s(k) \tag{53}$$

which yields the sensor output as follows:

$$\mathbf{x}_{sn}(k+1) = \mathbf{G}_{sn}\mathbf{x}_{sn}(k) + \mathbf{H}_{sn}\tilde{\mathbf{u}}_{sn}(k) \tag{54}$$

$$\mathbf{y}_{sn}(k+1) = \mathbf{C}_{sn}\mathbf{x}_{sn}(k) + \mathbf{D}_{sn}\tilde{\mathbf{u}}_{sn}(k) \tag{55}$$

The control law output, corresponding to each sampling time interval Δt_C is obtained as below using $\mathbf{y}_{sn}(k)$ from Eq. (55)

$$\mathbf{x}_c(k+1) = \mathbf{G}_c\mathbf{x}_c(k) + \mathbf{H}_c\mathbf{y}_{sn}(k) \tag{56}$$

$$\mathbf{y}_c(k) = \mathbf{C}_c\mathbf{x}_c(k) + \mathbf{D}_c\mathbf{y}_{sn}(k) \tag{57}$$

The desired control-surface motion is obtained from Eq. (57) and the actual motion of the control surface is obtained from the actuator transfer function,

$$\mathbf{x}_{ac}(k+1) = \mathbf{G}_{ac}\mathbf{x}_{ac}(k) + \mathbf{H}_{ac}\mathbf{y}_c(k) \tag{58}$$

$$\mathbf{y}_{ac}(k) = \mathbf{C}_{ac}\mathbf{x}_{ac}(k) + \mathbf{D}_{ac}\mathbf{y}_c(k) \tag{59}$$

with the control-surface motion being

$$\mathbf{y}_{ac}(k) = \begin{pmatrix} \mathbf{q}_{\delta 1} & \mathbf{q}_{\delta 2}, \ldots, & \dot{\mathbf{q}}_{\delta 1}, & \dot{\mathbf{q}}_{\delta 2}, \ldots, \end{pmatrix}^T \tag{60}$$

The position and velocity of the control surface are put back into the $\mathbf{x}_n$ vector which is the $\mathbf{x}_s$ vector with new control-surface definition.

The $\mathbf{u}$ and $\dot{\mathbf{u}}$ values are next calculated from $\mathbf{x}_n$ and modified to change the normal velocity boundary conditions at the solid boundary described earlier as the transpiration boundary condition. This is then followed by a one-step CFD solution using a global time-stepping scheme, and the entire solution process is then repeated for the required number of time steps. A time response solution of Eq. (48) in an interval ($\Delta t = t_{k+1} - t_k$) is obtained as

$$\mathbf{x}_s(k+1) = e^{\mathbf{A}_s\Delta t}\mathbf{x}_s(k) + \mathbf{A}_s^{-1}[e^{\mathbf{A}_s\Delta t} - \mathbf{I}]\mathbf{B}_s\mathbf{f}(\mathbf{k}) \tag{61}$$

The set of response data as above may be resolved into modal components using an FFT (fast Fourier transform), as

$$\mathbf{q} = \sum_{m=1}^{r} e^{\varsigma_m t}(a_m \cos\omega_m t + b_m \sin\omega_m t) \tag{62}$$

to yield the damping (ς) and frequency (ω) values. In practice, however, the generalized response is plotted against time. This plot depicting stability characteristic of the vehicle enables prediction of the onset of flutter or divergence occurring within the entire flight regime.

Another recent effort involving FE CFD analysis for unsteady flow has been described in [12]. The effect of aerodynamic heating [13] needs to be taken into consideration for the aeroelastic response

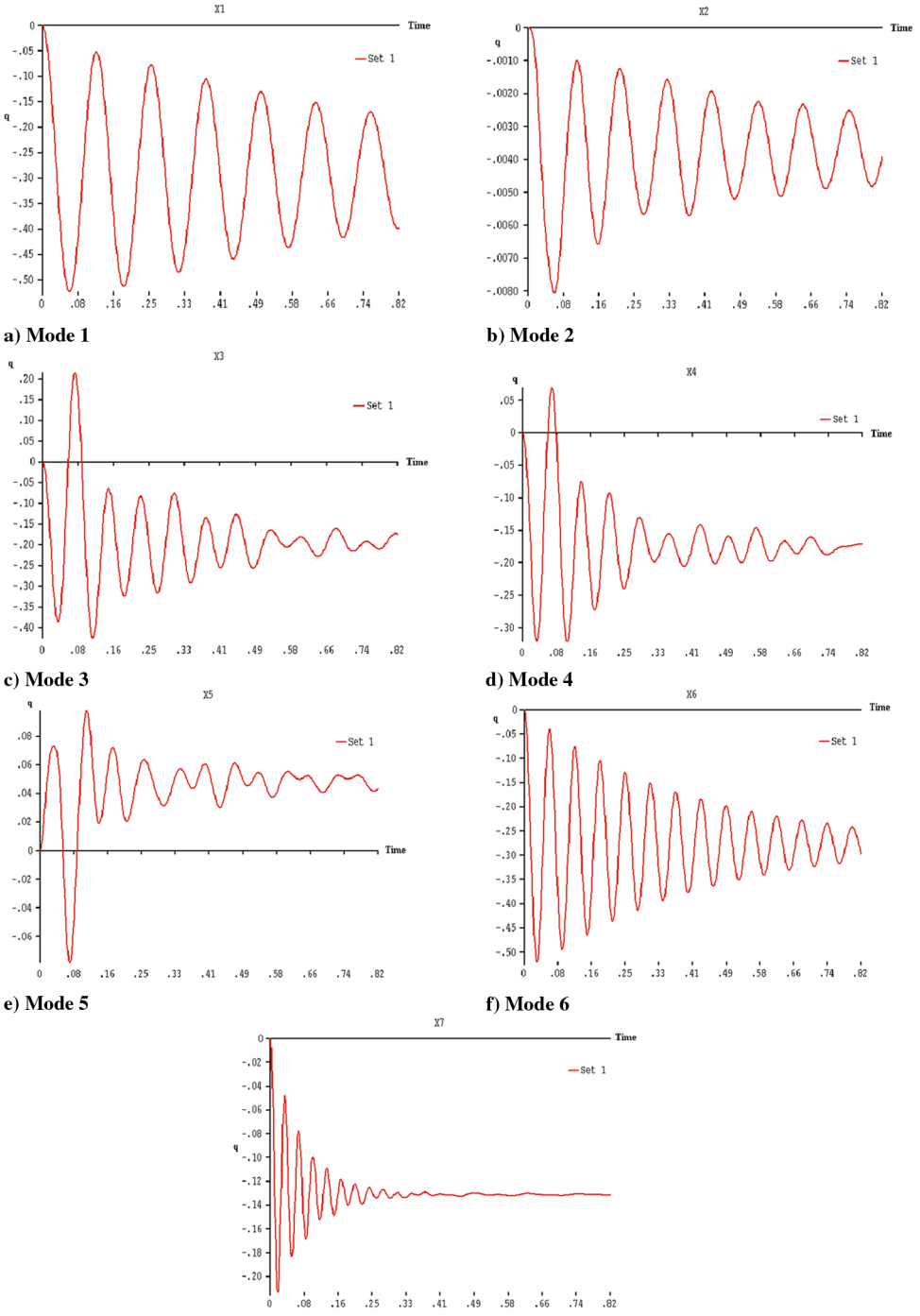

Fig. 17 Hyper-X generalized displacement response; Mach = 0.9, altitude = 22, 500 ft.

analysis of high speed vehicles. In this procedure, once the steady-state CFD analysis is completed, the temperature distribution at various heat transfer mesh node is obtained by interpolation from such data at aerodynamic grid points on the structural surface. Subsequent heat transfer analysis of the structure then yields the temperature distribution in all structural elements by suitable interpolation at structural nodes, and the stiffness matrix is next generated taking into account temperature-dependent material properties. Such a stiffness matrix is then used to perform a free vibration analysis, and the rest of the analysis continues as shown in Fig. 2.

This formulation allows for any digital control sampling rate that is different from the aeroelastic solution time steps. Such an analysis, pertaining to a specific Mach number, may then be repeated for a number of altitudes, involving various dynamic pressure values, and the instability altitude signified by a zero damping value may then be extracted using simple interpolation of each desired state variable.

Numerical Examples

An extensive number of relevant CFD examples [14,15] and also AE and ASE problems have been solved to assess the accuracy of the currently developed numerical formulation and software. An ASE analysis capability has also been verified with wind tunnel test results pertaining to the BACT (benchmark active controls technology) wing [9]. Examples of representative test problems are given next in which the CFDSOL (CFD solution) module of the STARS program has been used for the relevant CFD solutions. All example problems,

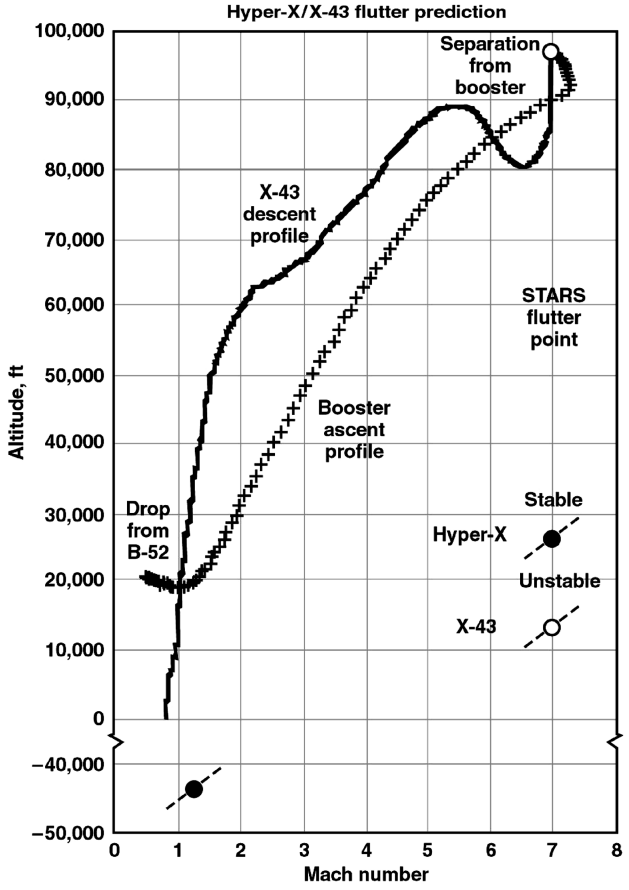

Fig. 18 Hyper-X typical AE response.

presented next, were solved using a 64 bits, single processor with clock speed of 3.19 GHz.

Example 1: Flow over NACA0012 Airfoil

The first example considered is the inviscid flow over a NACA0012 airfoil. The inlet Mach number of this flow is 1.2 and angle of attack is zero. About 1×10^6 unstructured tetrahedron elements were used for the analysis. Figure 4 depicts the distribution of calculated pressure and its comparison with the AGARD benchmark solution [14].

An extension of the problem, the viscous supersonic flow past a NACA0012 airfoil, is presented next in some detail. The details of the mesh used close to this solid surface are shown in Fig. 5. A total number of over 1×10^6 elements are used in this calculation. The inlet Mach number of this problem is assumed to be equal to 2. The airfoil surface is assumed to be solid and no slip flow conditions are assumed on the surface. Figure 6 shows the comparison of coefficient of pressure distribution along the chord surface between the present and the results obtained on an adapted mesh [15].

Example 2: AGARD Sweptback Wing 445.6

The wing configuration has a 45-deg, quarter-chord sweep angle and a NACA 65A004 airfoil section with a taper ratio of 0.66 and a panel aspect ratio of 1.65. Measured mode shapes and frequencies as well as wind tunnel flutter test results are available in the open literature [16,17]. The model referred to as the 25 ft weakened model 3 was selected for analysis and correlation. All results presented herein are based on inviscid flow.

A finite element model for the wing yields the first four natural frequencies as 9.60, 38.20, 48.35, and 91.54 Hz, corresponding to the first bending, first torsion, second bending, and second torsion modes, respectively. Such data were used for subsequent simulation of flutter characteristics of the wing at freestream Mach numbers 0.499, 0.678, 0.901, 0.96, 1.072, and 1.140, respectively, to afford comparison with test data, thereby validating the numerical simulation capability described herein. Pertaining to each Mach number, aeroelastic responses were computed for several representative values of dynamic pressure to bracket the flutter points. The inclusion of higher modes in the study did not result in an appreciable difference in the solution results.

The aerodynamic grid (Fig. 7) for the CFD Euler solution consists of 45,145 nodes and 239,709 tetrahedron elements. For time-marching unsteady calculations, the global time step is $\Delta t = 0.00027378$ and a damping coefficient was taken as 0.02 for all test cases. Special care was taken to generate a finer mesh in the vicinity of the airfoil to yield an accurate solution. For transonic and low supersonic flow, an enhanced grid consisting of 69,630 nodes and 373,798 elements was used for the relevant analyses. Such a refined grid was necessary to enable capture of shocks in the transonic flow

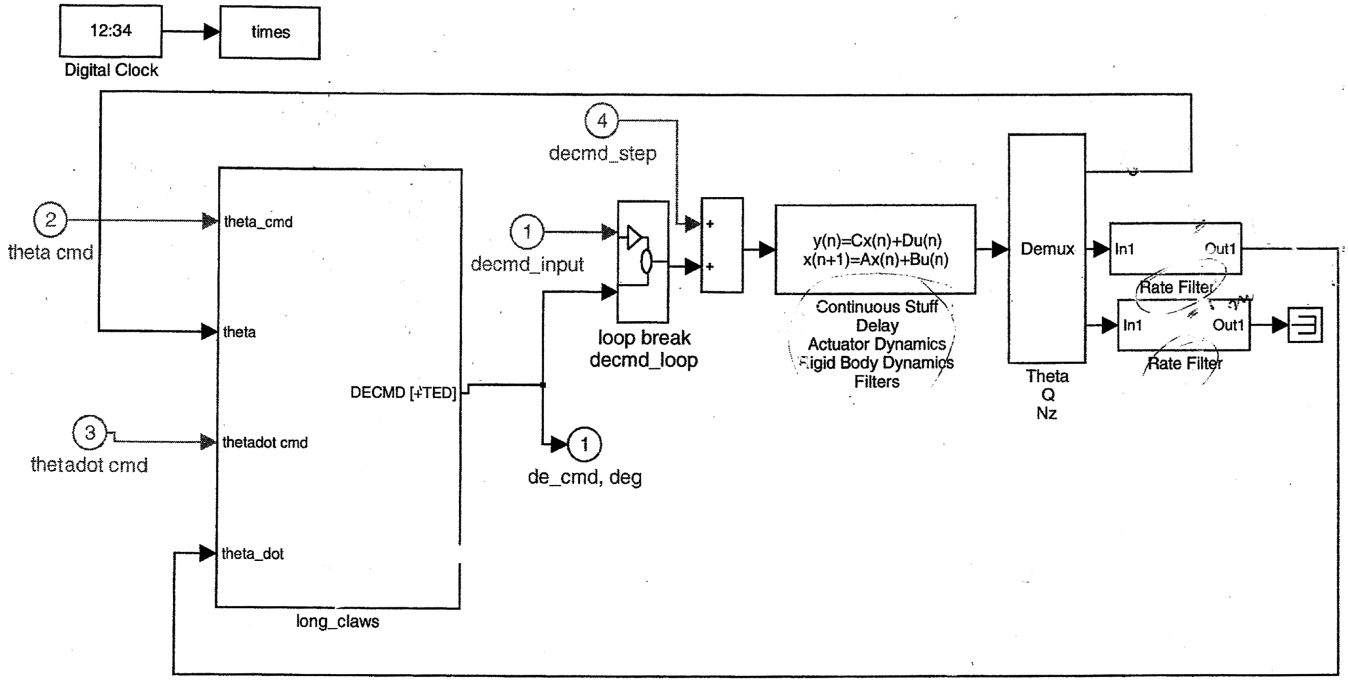

Fig. 19 Hyper-X longitudinal control law.

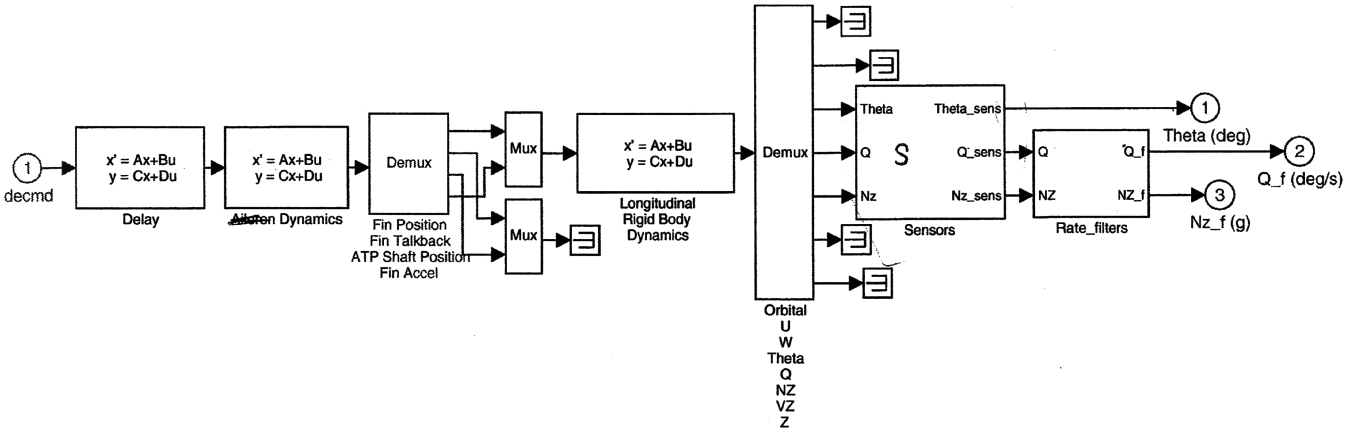

Fig. 20 Hyper-X plant.

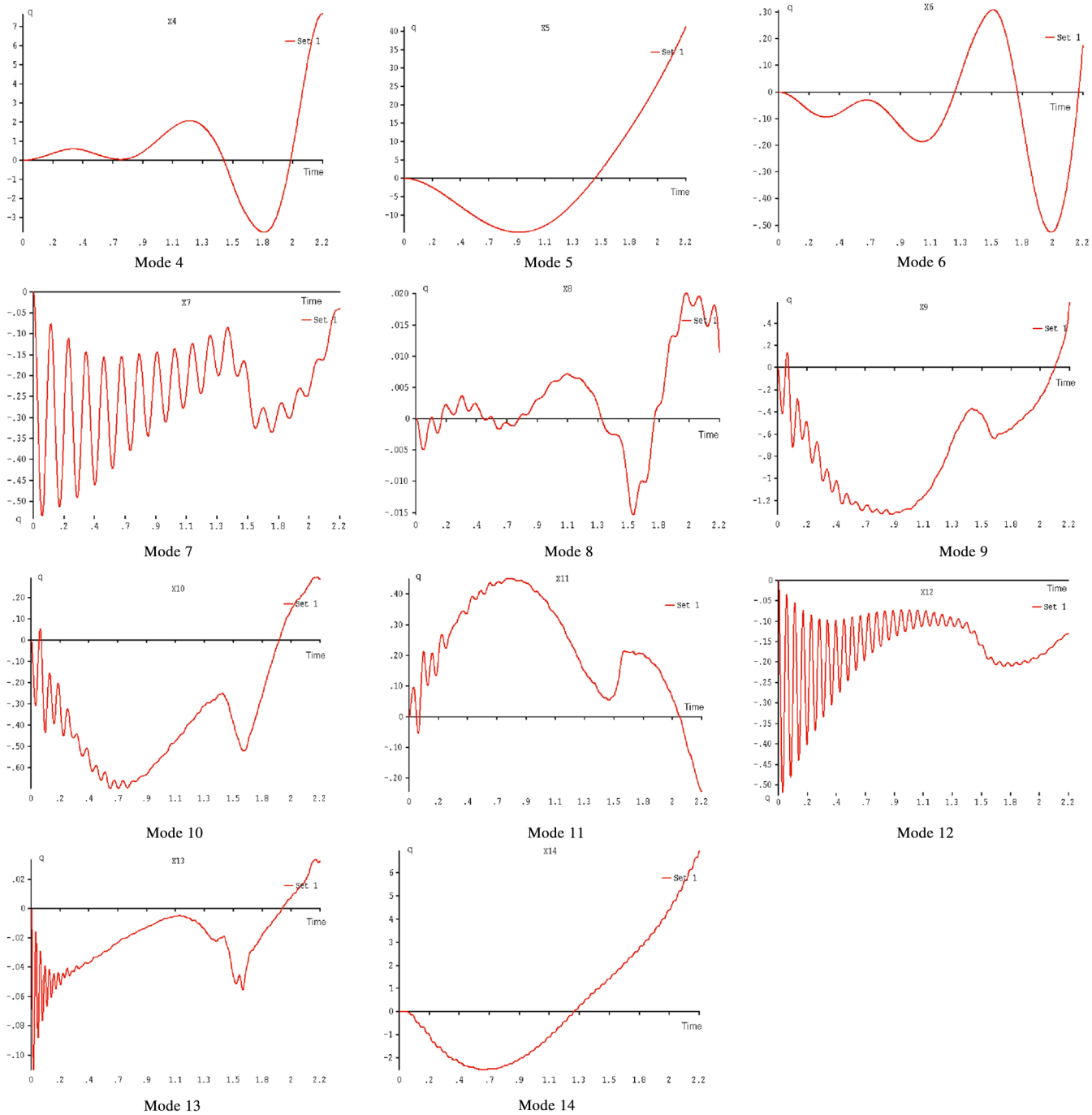

Mode 4 Mode 5 Mode 6

Mode 7 Mode 8 Mode 9

Mode 10 Mode 11 Mode 12

Mode 13 Mode 14

Fig. 21 Hyper-X flight vehicle ASE generalized displacement (q) responses.

regime. Table 1 presents a comparison of calculated and test [16,17] results. Figure 8 provides a pictorial depiction of such results along with a solution derived by using a higher order method [18]; excellent correlation is shown between the currently calculated results and the test data, throughout the entire flight regime including transonic flow. All calculations were made using a 3.19 GHz, 64 bits PC that required CPU time of about 1.25 h for a steady-state solution per flight point; relevant CPU time for unsteady simulation is typically about 7–8 h; grid generation time amounted to around 3 min.

Example 3: Hyper-X Flight Vehicle

The Hyper-X stack, Fig. 9, consists of a Pegasus booster and the X-43 hypersonic flight test vehicle, which are launched from a B-52 aircraft as shown in Fig. 10 [1]. Once the vehicle is boosted to around 100,000 ft, the X-43 separates from the booster and is designed to perform a hypersonic free flight at Mach 7 and also at about Mach 10. Stability analysis of the X-43 and the stack at Mach 7 was described in [2,3], respectively. A related analysis of the stack in the transonic flight regime is of critical importance for the success of the project and a representative solution is presented herein. A finite element structural model consists of 20,017 nodes and a total of 22,420 various elements resulting in an approximate 120,000 degrees of freedom dynamic problem. Figure 11 shows the finite element structural model whereas the first few typical mode shapes are shown in Fig. 12. Table 2 provides a list of natural frequencies identifying the choice of modes for aeroservoelastic as well as aeroelastic analysis; this was based on numerous studies on modal convergence. A progressive simultaneous iteration method [19] was used for the eigensolution requiring about 6 min of CPU time for the extraction of the first 20 roots and vectors. The angles of attack for the vehicle and the horizontal tails were taken as 12.43 and −11 deg, respectively.

Stability analyses of the vehicle were performed at Mach 0.9, at an altitude of 22,500 ft, employing selective modes 7, 8, 11–13, 15, and 21, respectively. Details of aerodynamic mesh are shown in Fig. 13 consisting of 496,526 nodes and 2,653,975 tetrahedron elements, which is a 2.5 million degree of freedom problem. Mach and pressure distributions pertaining to a steady-state analysis are shown in Fig. 14, indicating aeroelastic stability. A comparison of flight measured values of aerodynamic pressure data with CFD computed results, pertaining to inviscid flow (high Reynolds number, around 10^{15}) is given in Table 3 and graphically depicted in Fig. 15; excellent correlation is observed for the primary data values; the last three pressure values in the table are rather small and hence prone to measurement inaccuracy. The relevant sensor locations are shown in Fig. 16. Distribution of generalized displacements for the AE analysis, pertaining to a few representative elastic modes, is shown in Fig. 17. A summary of predicted flutter points [20], along the flight trajectory, for Hyper-X and the X-43, defining the flutter boundary is shown in Fig. 18.

A detailed coupled aeroservoelastic analysis (Fig. 3) at Mach 0.9 was conducted for the critical flight condition to assess the aerostructural-controls stability by calculating the longitudinal closed-loop response. The relevant details of the control law are shown in Fig. 19 and also in Fig. 20. Figure 21 depicts the generalized response plots of a few typical modes, depicting possible ASE instability. An associated analysis indicated that rigid-body dynamics is unstable in the open loop model.

The steady-state CFD solution took about 10 h and the associated unsteady solution needed around 200 h of CPU time, using the 64 bit single processor PC with a clock speed of 3.19 GHz.

Concluding Remarks

This paper, an expanded and modified version of [21], presents details of a new finite element, CFD-based aeroservoelastic analysis procedure suitable for modeling and simulation of large complex practical problems. A novel CFD and a new direct time marched analysis procedure are described in detail, along with the unique Hyper-X simulation results.

Numerical examples include the NACA0012 airfoil and the current solutions are compared to earlier ones for both inviscid as well as viscous flow. The second example involves the AGARD sweptback wing 445.6 and related aeroelastic wind tunnel test results are compared with current numerical analysis results that are found to be quite favorable. Finally, results of vibration, aeroelastic, and aeroservoelastic analyses of the novel Hyper-X launch vehicle are presented in detail. Also presented is a comparison of computed pressure values with flight test data. These results testify to the accuracy and efficiency of the numerical techniques presented herein.

The use of CFD techniques for the accurate prediction of unsteady aerodynamic forces around a flight vehicle is essential for transonic flow conditions [22,23]. The employment of linear panel methods for such a simulation will generally prove to be unreliable. For large, complex practical problems, parallelization of relevant analysis codes employing multiple processors is expected to bring down solution time quite considerably and future effort is being directed to that effect. References [24,25] provide detailed review of state-of-the-art developments of associated research efforts.

Acknowledgments

Thanks are due to S. Lung, E. Hahn, T. Doyle, C. L. Lawson, and P. Nithiarasu for their sincere help in the preparation of this work.

References

[1] Ko, W. L., and Gong, L., "Thermostructural Analysis of Unconventional Wing Structures of a Hyper-X Hypersonic Flight Research Vehicle for the Mach 7 Mission," NASA TP-2001-210398, 2001.

[2] Gupta, K. K., Voelker, L. S., Bach, C., Doyle, T., and Hahn, E., "CFD Based Aeroelastic Analysis of the X-43 Hypersonic Flight Vehicle," AIAA Paper 2001-0712, 8–11 Jan. 2001.

[3] Gupta, K. K., Voelker, L. S., and Bach, C., "Finite Element CFD Based Aeroservoelastic Analysis," AIAA Paper 2002-0953, 14–17 Jan. 2002.

[4] Lighthill, M. J., "On Displacement Thickness," *Journal of Fluid Mechanics*, Vol. 4, 1958, pp. 383–392.

[5] Sankar, L. N., Malone, J. B., and Schuster, D., "Euler Solutions for Transonic Flow Past a Fighter Wing," *Journal of Aircraft*, Vol. 24, No. 1, 1987, pp. 10–16.

[6] Donea, J., "A Taylor-Galerkin Method for Convective Transport Problem," *International Journal of Numerical Methods in Engineering*, Vol. 20, No. 1, 1984, pp. 101–119.

[7] Peraire, J., Peiro, J., Formaggia, L., Morgan, K., and Zienkiewicz, O. C., "Finite Element Euler Computations in Three Dimensions," *International Journal of Numerical Methods in Engineering*, Vol. 26, No. 10, 1988, pp. 2135–2159.

[8] Spalart, P. R., and Allmaras, S. R., " A One-Equation Turbulence Model for Aerodynamic Flows," AIAA Paper 92-0439, 1992.

[9] Gupta, K. K., and Meek, J. L., *Finite Element Multidisciplinary Analysis*, 2nd ed., AIAA Education Series, AIAA, Reston, VA, Sept. 2003.

[10] Gupta, K. K., "STARS—An Integrated General-Purpose Finite Element Structural, Aeroelastic and Aeroservoelastic Analysis Computer Program," NASA TM 4795, May 1997, revised March 2004 (Ver. 04/01).

[11] Gupta, K. K., "Development of a Finite Element Aeroelastic Analysis Capability," *Journal of Aircraft*, Vol. 33, No. 5, 1996, pp. 995–1002.

[12] Geuzaine, P., Brown, G., and Farhat, C., "Three Fields Based Nonlinear Aeroelastic Simulation Technology: Status and Application to the Flutter Analysis of an F-16 Configuration," AIAA Paper 2002-0870, 2002.

[13] Heeg, J., Zeiler, T., Pototzky, A., Spain, V., and Engelund, W., "Aero Thermoelastic Analysis of a NASP Demonstrator Model," AIAA Paper 93-1366, 1993.

[14] Pullian, T. H., and Barton, J. T., "Euler Computations of AGARD Working Group 07 Aerofoil Test Cases," *AIAA 23rd Aerospace Science Meeting*, AIAA, New York, Jan. 1985.

[15] Castro-Diaz, M. J., Hecht, F., and Mohammadi, B., "Anisotropic Unstructured Mesh Adaptation for Flow Simulation," *Finite Elements in Fluids Conference*, 1995.

[16] Yates, E. C., Jr., Land, N. S., and Fougher, J. T., "Measured and Calculated Subsonic and Transonic Flutter Characteristics of a 45 Swept-Back Wing Planform in Air and in Freon-12 in the Langley Transonic Dynamics Tunnel," NASA TN D-1616, March 1963.

[17] Yates, E. C., Jr., "AGARD Standard Aeroelastic Configuration for Dynamic Response, Candidate Configuration 1.—Wing 445.6," NASA TM-100492, Aug. 1987; also *Proceedings of the 61st Meeting of the Structures and Materials Panel*, AGARD R-765, 1985 pp. 1–73.

[18] Lesoinne, M., and Farhat, C., "Higher-Order Subiteration-Free Staggered Algorithm for Nonlinear Transient Aeroelastic Problems," *AIAA Journal*, Vol. 36, No. 9, 1998, pp. 1754–1756.

[19] Gupta, K. K., and Lawson, C. L., "Structural Vibration Analysis by a Progressive Simultaneous Iteration Method," *Proceedings of the Royal Society of London, Series A: Mathematical and Physical Sciences*, Vol. 455, 1999, pp. 3415–3424.

[20] Gupta, K. K., Voelker, L. S., Bach, C., Doyle, T., and Hahn, E., "CFD Based Aeroelastic Analysis of the X-43 Hypersonic Flight Vehicle," AIAA Paper 2001-0712, Jan. 2001.

[21] Gupta, K. K., Bach, C., Doyle, T., and Hahn, E., "CFD-Based Aeroservoelastic Analysis with Hyper X Application," AIAA Paper 2004-884, Jan. 2004.

[22] Gupta,K. K., "Development and Application of an Integrated Multidisciplinary Analysis Capability," *International Journal for Numerical Methods in Engineering*, Vol. 40, 1997, pp. 533–550.

[23] Geuzaine, P., Brown, G., Harris, C., and Farhat, C., "Aeroelastic Dynamic Analysis of A Full F-16 Configuration for Various Flight Conditions," *AIAA Journal*, Vol. 41, No. 3, March 2003, pp. 363–371.

[24] Friedmann, P. P., "Renaissance of Aeroelasticity and Its Future," *Journal of Aircraft*, Vol. 36, No. 1, 1999, pp. 105–121.

[25] Livne, E., "Integrated Aeroservoelastic Optimization: Status and Direction," *Journal of Aircraft*, Vol. 36, No. 1, 1999, pp. 122–143.

E. Livne
Associate Editor